UMERC+OREC
2025 Conference
12–14 August — Corvallis, OR USA

Numerical Simulation-Based Performance and Loading Assessment of a Dual-Rotor Ocean Current Turbine Operating in the Florida Straits

Hassan Mokari[a], James VanZwieten[b], Yufei Tang[a], John Sninsky[c]

[a]Florida Atlantic University, Department of Electrical Engineering and Computer Science, 777 Glades Road, Boca Raton, FL 33431, USA
[b]Florida Atlantic University, Department of Ocean and Mechanical Engineering, 101 North Beach Road, Dania Beach, FL 33004, USA
[c]Current Kinetics, LLC, 10823 SW 27th Ave., Gainesville, Florida, USA

Abstract:

Ocean currents present along the western boundaries of global ocean basins represent a significant renewable energy resource, with localized energy densities off the east coast of the US exceeding 3 kW/m^2 in areas and a total extractable potential in the gigawatt range. Most energy-rich currents are located within the upper 100 meters of the water column in areas where total depths exceed 250 meters. To harness this energy efficiently, moored ocean current turbines (OCTs) are being investigated that use variable buoyancy control, lifting surfaces, or a combination of both for depth regulation. This research focuses on a dual-rotor OCT configuration that utilizes both variable buoyancy and lifting surfaces, such that the variable buoyancy controls the pitch of the system, which in turn impacts the lift force on a wing structure, controlling the operating depth. This study presents a numerical simulation-based performance assessment of a dual-rotor OCT operating in the Florida Straits. The turbine dynamics are modeled using a rigid-body framework with eight degrees of freedom, six associated with the main body and two corresponding to the independent rotational speeds of the dual rotors. Additionally, the mooring system is represented through a finite-element, lumped-mass cable model, where each node is assigned three degrees of freedom. The findings provide insights into the dynamic response and power production of the proposed turbine configuration under various ballast tank fill distributions and flow conditions. Specifically, open-loop simulations are conducted for (i) different buoyancy tank fill levels at constant flow speed and zero turbulence, and (ii) different flow speeds with identical tank fill levels and no turbulence. Additionally, closed-loop results are presented for varying flow speeds under a fixed fill configuration with 10% turbulence.

Keywords: Renewable Energy, Ocean Current Energy, Ocean Current Turbines, Marine Current Turbines, Numerical Simulation

1. Introduction

The pursuit of sustainable electricity generation has intensified global interest in renewable energy sources such as wind, solar, tidal, wave, and ocean currents. Among these resources, ocean currents offer the distinct advantage of high temporal stability and relatively steady power output [1]. Despite this promise, the technological maturity of ocean current energy systems remains limited, and significant engineering and environmental challenges must be addressed to make large-scale deployment viable [2]. Globally, the most prominent ocean currents include the Gulf Stream, Brazil currents in the Atlantic, Agulhas current in the Indian Ocean, and Kuroshio current in the Pacific [3]. In particular, the Gulf Stream, a key component of the Atlantic Meridional Overturning Circulation, offers substantial extractable energy, with theoretical estimates suggesting approximately 44 GW [4], including around 5 GW from the Florida Current alone [5]. These values are derived from simplified ocean circulation models that account for the potential feedback of energy extraction on current dynamics. Energy density is strongly correlated with depth, with the highest energy densities occurring near the ocean surface [6]. Consequently, optimal turbine deployment typically favors near-surface installations. However, adaptability in

turbine depth can offer operational advantages. Variable-depth capabilities allow turbines to avoid extreme surface conditions during storms and enable operation below shipping traffic. This study presents a numerical investigation of the hydrodynamic performance and structural loading of a dual-rotor OCT designed for operation in the Florida Straits. The turbine features a combined variable-buoyancy and lift-based depth control mechanism, enabling active depth control in a dynamic ocean environment.

2. Ocean Current Turbine Modeling

The numerical simulations presented in this study extend the methodologies introduced in [5]–[7], with advancements in the equations of motion and actuator modeling. This section provides a summary of the dual-rotor OCT model, encompassing the coordinate frameworks, dynamic equations, blade element momentum (BEM) rotor theory, additional hydrodynamic force representations, and environmental interaction models.

Table 1: Key Properties of Baseline OCT

Dimension	Unit	Value
Moment of Inertia I_x	kgm^2	4.66×10^7
Moment of Inertia I_y	kgm^2	1.46×10^6
Moment of Inertia I_z	kgm^2	4.72×10^7
Rotor Inertia (each)	kgm^2	1.87×10^5
Total Mass m	kg	218,680
Buoyancy Tank Mass	kg	41,642
CG - CB [x,y,z]	m	[−0.0023, 0, 0.057]
Generator Mass	kg	53,669
Main Wing Mass	kg	34,594
Cable Attach Pt. (CAP)	m	[2.72, 0, 2]
Cable Length	m	607
Cable Diameter D_c	m	0.16

Table 2: Structural Parameters of Baseline OCT

Dimension	Unit	Value
Buoyancy Tank Volume	m^3	40
Buoyancy Tank Length	m	15
Ballast Section Length	m	6
Electronics Section Length	m	3
Tank Diameter	m	2.2
Generator Outer Diameter	m	6
Generator Inner Diameter	m	4
Generator Length (front–back)	m	4
Rotor Diameter D_r	m	20
Wing Thickness	m	0.6
Main Wing Span (each)	m	15
Main Wing Chord	m	5

2.1 Overview of Simulated OCT

While the configuration builds upon the lifting-surface-controlled OCT concept introduced in [5], it is modified to eliminate the need for active wing control. In this design, the lifting surfaces are integrated rigidly with the surrounding structure, eliminating the need for direct actuation. Instead, a buoyancy tank, comprising two independent chambers, is utilized to modulate the total system mass and center of mass (accounting for entrained water) to vary the turbine's overall pitch, thereby influencing the lift generated by the main wing. A schematic of this configuration is provided in Fig. 1 (not to scale). The system features two generators mechanically connected via a central main wing spanning a total length of 30 meters across both sections. Between these two 15-meter wing section is the variable buoyancy tank. Additionally, a 607-meter mooring cable anchors the turbine from the seabed to the base of the buoyancy tank. Table 1 and Table 2 summarize the key physical and inertial properties of the baseline dual-rotor OCT, including the system's total mass, moments of inertia, component dimensions, and structural parameters necessary for dynamic modeling and simulation.

2.2 Equations of Motion

The motion of the numerically simulated OCT is described using 8 degrees of freedom (DOFs). The equations of motion for the 6-DOF movement of the main body (excluding the rotors) of the OCT system were derived from [7]. These 6-DOF accelerations include the OCT's linear accelerations $\dot{u}, \dot{v}, \dot{w}$ and angular accelerations $\dot{\omega}_x, \dot{\omega}_y, \dot{\omega}_z$:

$$\begin{bmatrix} \dot{u} \\ \dot{v} \\ \dot{w} \end{bmatrix} = m^{-1} F \begin{bmatrix} i_{\bar{B}} \\ j_{\bar{B}} \\ k_{\bar{B}} \end{bmatrix} + \begin{bmatrix} u \\ v \\ w \end{bmatrix} \times \begin{bmatrix} \omega_x \\ \omega_y \\ \omega_z \end{bmatrix}$$

$$\begin{bmatrix} \dot{\omega}_x \\ \dot{\omega}_y \\ \dot{\omega}_z \end{bmatrix} = \begin{bmatrix} I_x^{-1} & 0 & 0 \\ 0 & I_y^{-1} & 0 \\ 0 & 0 & I_z^{-1} \end{bmatrix} \left(M \begin{bmatrix} i_{\bar{B}} \\ j_{\bar{B}} \\ k_{\bar{B}} \end{bmatrix} - \begin{bmatrix} (I_z - I_y)\omega_y\omega_z \\ (I_x - I_z)\omega_z\omega_x \\ (I_y - I_x)\omega_x\omega_y \end{bmatrix} \right)$$

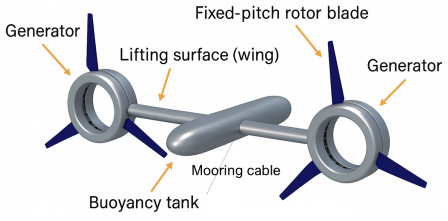

Fig. 1: Schematic diagram of the dual-rotor ocean current turbine.

where F denotes the total external force vector expressed in the body-fixed frame ($\bar{B}$), M represents the vector of applied moments about the center of gravity, and m shows the total mass of the turbine. These force and moment vectors encompass all external contributions acting on the system, except for the moment about the longitudinal (x) axis. In that case, the hydrodynamic torque τ_x^r on the two rotors is replaced by the electromechanical torques (τ_x^e) generated by the twin rotor generators. The rotational velocities about the body-fixed x, y, and z axes are represented by ω_x, ω_y, and ω_z, respectively. The total force F acting on the OCT consists of multiple components: the gyroscopic force F_G, the combined gravitational and buoyant force F_{gb}, the lift and drag forces generated by the two wings F_w, the hydrodynamic forces on the two rotors F_r, the hydrodynamic forces on the two generators F_g, and the tether (cable) force F_c, such that:

$$F = F_G + F_{gb} + \sum_{m=1}^{2} F_{w,m} + \sum_{m=1}^{2} F_{r,m} + F_c + F_g \tag{1}$$

The final 2-DOF of this OCT are the rotational velocities of both rotors about the x-axis. The rotational acceleration of each rotor is calculated as follows:

$$\dot{\omega}_x^r = \frac{\tau_x^r + \tau_x^e - \omega_y \omega_z (I_z^r - I_y^r)}{I_x^r} \tag{2}$$

where I_x^r, I_y^r, and I_z^r denote the moment of inertia of each rotor about the x-axis, y-axis, and z-axis, respectively; ω_y is the rotational velocity about the y-axis, and ω_z determines the rotational velocity about the z-axis. Finally, the overall DOFs for the modeled system include three translational DOFs for each cable node in the cable model.

3. Open-Loop Analysis

This section presents an open-loop analysis of the dynamic response of the dual-rotor OCT. The system's behavior is evaluated in response to step changes in buoyancy tank fill levels and ocean current speeds. Key performance metrics, such as depth, pitch angle, and electrical power output, are analyzed to provide insight into the system's response under uncontrolled operating conditions. It is important to note that the main wings are statically pitched at $+4^\circ$, which closely corresponds to the angle of maximum lift for typical hydrofoil sections. Stall onset generally occurs beyond $+15^\circ$, depending on the hydrofoil geometry and Reynolds number. As shown in Fig. 2, all pitch angles remain within the narrow range of approximately -0.4° to $+0.6^\circ$, well below the stall threshold, except for the (0%, 100%) configuration. Therefore, under these conditions, none of the buoyancy fill configurations induce stall on the main wing, except for (0%, 100%), which may approach or exceed the stall angle depending on dynamic effects.

3.1 Evaluation of Response to Different Buoyancy Tank Fill Level

The dynamic response of the OCT is evaluated under a depth-independent flow field with a mean velocity of $1.6\,\mathrm{m/s}$ and without the influence of waves or turbulence. Initially, the turbine is positioned near its equilibrium depth of $75\,\mathrm{m}$ with both ballast tanks filled to 50% of their capacity (i.e., $10\,\mathrm{m}^3$ each). After 120 seconds step adjustments are made to the fill levels to assess system behavior under the following seven ballast configurations: (0%, 0%), (50%, 50%), (25%, 75%), (75%, 25%), (100%, 0%), (0%, 100%), and (100%, 100%). Fig. 2 presents the time histories of depth (Top), pitch angle (Middle), and power production (Bottom). As the baseline case, both tank fill levels remain at 50% during one simulation, and the turbine is near the target depth of approximately 75 meters.

To evaluate the response due to simultaneous changes in fill levels, step changes to (0%, 0%) and (100%, 100%) are evaluated. After 18 minutes, OCT depth nearly achieves equilibrium with values of $15\,\mathrm{m}$ for (0%, 0%) and $153\,\mathrm{m}$ for (100%, 100%). Furthermore, the variation of pitch angle for each configuration is presented in Fig. 2 (Middle). The pitch angle remains near zero and highly stable in the symmetric baseline case (50%, 50%), with a final value of approximately -0.095° and a peak value of 0.221°, indicating a level attitude during operation. In contrast, the (0%, 0%) and (100%, 100%) cases yield final pitch angles of -5.153° and $+5.83^\circ$, respectively, reflecting sustained bow-down and bow-up orientations due to unbalanced cable moments

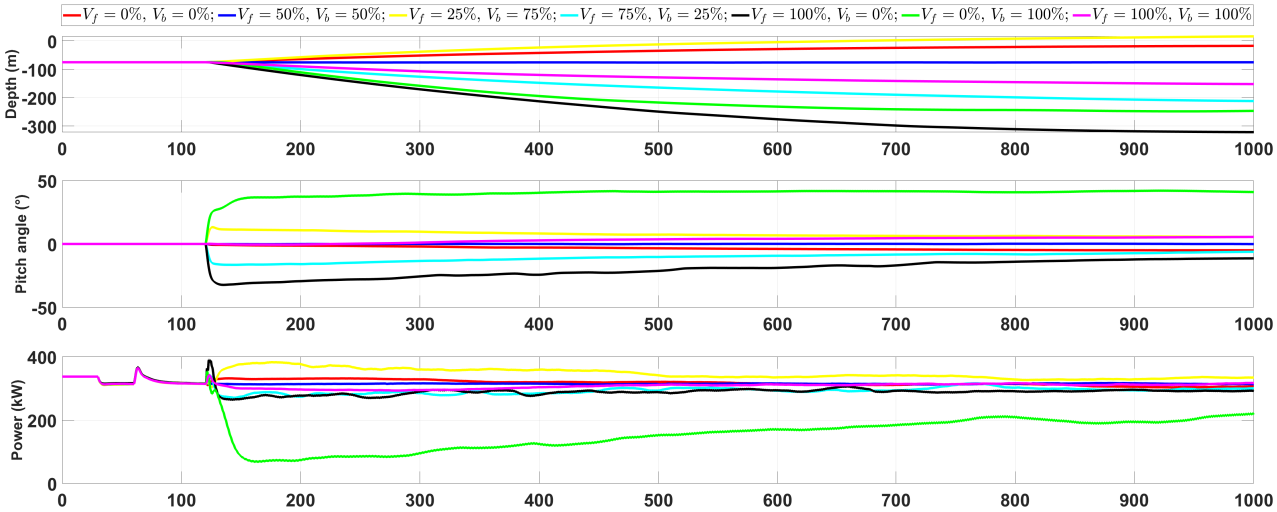

Fig. 2: (Top) OCT (negative) depth [m], (Middle) Pitch angle [deg], and (Bottom) Power production [kW], and for 20-minute simulations where ballast tank fill levels are altered after the first 2 minutes.

Table 3: Final depth, pitch angle, and power output for various buoyancy tank fill configurations.

Fill Configuration	**Final depth (m)**	**Final Pitch angle (°)**	**Peak Power (kW)**	**Final Power (kW)**
(0%, 0%)	-17	-5	363	306
(75%, 25%)	-211	-6	363	305
(25%, 75%)	16	6	382	320
(0%, 100%)	-246	40	346	230
(100%, 0%)	-320	-11	390	290
(50%, 50%)	-75	0	366	314
(100%, 100%)	-151	6	365	313

associated with the modified operating depth. For these two cases, (0%, 0%) and (100%, 100%), the peak pitch angles are equal to their final values, indicating steady-state behavior and that both cases do not induce stall on the main wing structure.

More critically, configurations with identical total fill levels but differing distributions, such as (25%, 75%) versus (75%, 25%), yield distinctly different depth trajectories due to the induced hydrostatic moments. When more water is concentrated in the front tank, the turbine experiences a nose-down moment and sinks more rapidly. In contrast, rear-weighted cases result in a nose-up orientation, promoting lift and upward motion. These outcomes highlight the importance of both the magnitude and distribution of ballast water in determining the vertical stability of the system. For the asymmetric buoyancy distributions, the (25%, 75%) case exhibits a final depth of $16\,m$, a peak pitch angle of 13° and settles at a final value of 6°, indicating a pronounced and sustained nose-up orientation. Conversely, the (75%, 25%) case shows a final depth of -211 m, no initial overshoot in its pitch angle, maintaining a peak of 0°, but converges to a final pitch angle of -6°, reflecting a persistent bow-down attitude.It is important to assess whether any of these positive pitch angles approach or exceed the static stall threshold of the main wing. In the (25%, 75%) case, although the peak pitch angle reaches 13°, this remains below the typical stall onset range (commonly around 15° for hydrofoils), suggesting that stall is unlikely to occur under the observed conditions.

As the fill levels become increasingly asymmetric, pitch angles deviate significantly. For example, front-loaded configurations such as (100%, 0%), with a peak pitch angle of 0° and a final value of -11°, lead to a pronounced nose-down orientation. In contrast, rear-loaded setups such as (0%, 100%) exhibit a final depth of -246 m with a peak pitch angle of 42° and a final value of 41°, resulting in a sustained nose-up attitude. These deviations are directly attributed to uneven buoyant forces distributed along the longitudinal axis of the turbine, emphasizing

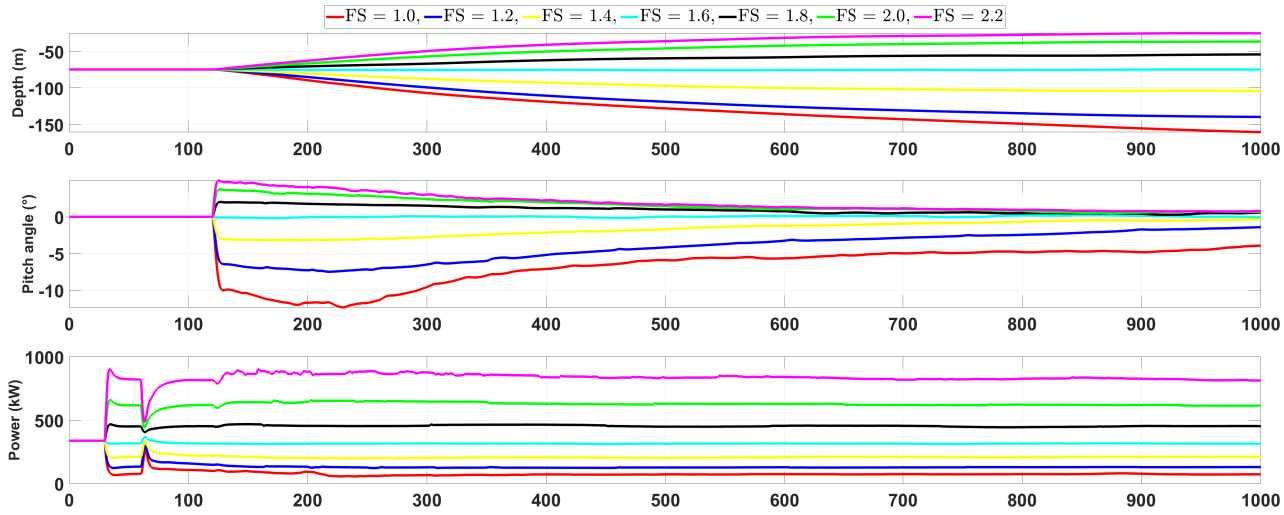

Fig. 3: Comparing (Top) OCT (negative) depth [m], (Middle) Pitch angle [deg], and (Bottom) Power production [kW], and for 20-minute simulations for different flow speeds.

the sensitivity of pitch dynamics to the front–rear ballast ratio. The configuration (0%, 100%), which shows a final depth of -320 m, results in a pitch angle of the main wing well beyond the stall, greatly increasing the drag and decreasing the lift on the main wing, both of which induce downward motions in the OCT. This pitch also creates a major misalignment between the rotor and the flow, as illustrated in Fig. 2 (Bottom), greatly reducing the power output.

These findings highlight the importance of using ballast to control wing pitch angles within aerodynamic limits to prevent stall, ensure smooth dynamics, and preserve turbine performance. Maintaining small pitch angles is also important for maximizing power production, as depicted in Fig. 2 (Bottom). This demonstrates the coupling between buoyancy control and energy harvesting efficiency and suggests that ballast regulation can serve as a viable control input for optimizing real-time turbine output. Table 3 summarizes the final depth, pitch angle, and power output for various buoyancy tank fill configurations. The data clearly demonstrate how different fill levels affect the turbine's orientation and energy performance. These results highlight the trade-off between stability and power generation across different buoyancy distributions.

3.2 Evaluation of Response to Different Flow Speeds

This section investigates the response of the OCT to step changes in flow speed where ballast levels are held constant at 50% for each tank. Fig. 3 shows the open-loop response of the dual-rotor OCT system is evaluated under varying flow speeds over 20-minute simulation periods. In the top subplot, the depth-time curves reveal that higher flow speeds (e.g., 2.0 and 2.2 m/s) result in higher operating altitude (decreased depth) as increased hydrodynamic lift counteracts gravitational and buoyancy forces. Conversely, lower flow speeds (e.g., 1.0 to 1.4 m/s) lead to a steeper downward trajectory, indicating reduced lift and increased net downward force. The middle subplot shows corresponding pitch angle responses, where higher flow speeds yield increasingly positive pitch angles while lower flow speeds result in increasingly negative values, signifying a nose-down attitude. The bottom subplot illustrates that power generation increases consistently with flow speed, with the highest power output observed at 2.2 m/s, reaching nearly 900 kW. At lower speeds, both power magnitude and stability are reduced due to weaker flow-induced torque and unsteady turbine alignment.

4. Control System

The control system component of the dual-rotor OCT is conducted by a designed Proportional-Integral (PI) controller. This controller dynamically regulates the volumes of the front and back buoyancy tanks to stabilize

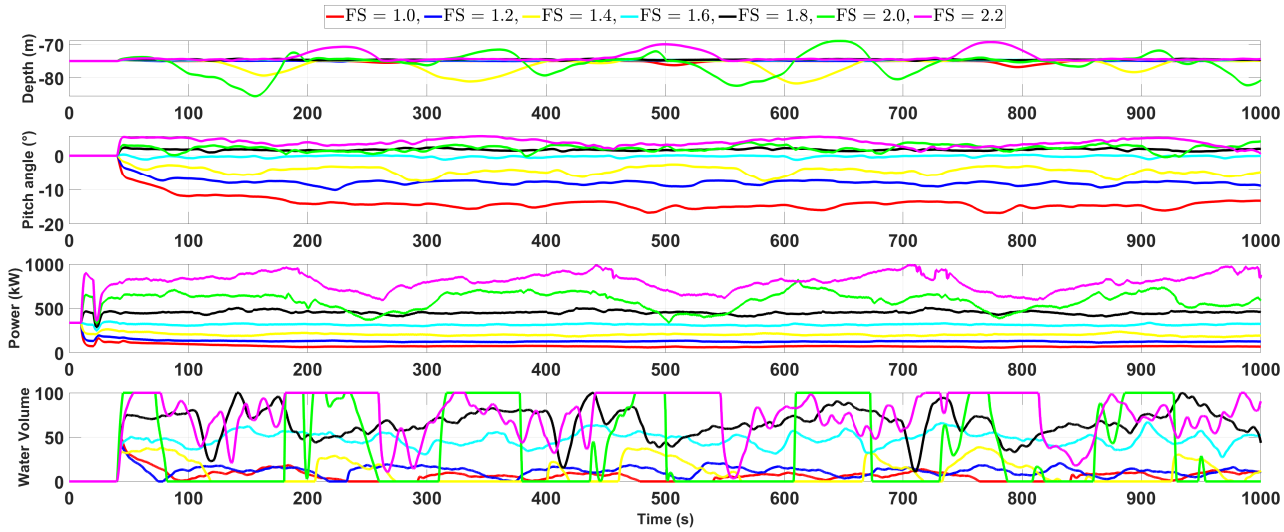

Fig. 4: Comparison of (Top) OCT depth [m], (Second) pitch angle [deg], (Third) total power production [kW], and (Bottom) the fill levels of both fore and aft buoyancy tanks [%] for 20-minute closed-loop simulations under varying flow speed profiles. All cases assume identical ballast tank fill levels and a 10% turbulence intensity. Time references the 6-DOF simulation run, which starts at 120 seconds.

the turbine at a desired operating depth. The dynamic of the PI controller is defined as follows.

$$u(t) = K_p \left(z_{\text{ref}} - z(t)\right) + K_i \int_0^t \left(z_{\text{ref}} - z(t)\right) dt \tag{3}$$

where z_{ref} is the desired reference depth, and $z(t)$ is the measured depth at time (t). K_p is the proportional gain and K_i is the integral gain. The control output $u(t)$, which adjusts the fill level of the buoyancy tanks, is constrained between 0% and 100% to reflect physical tank limits.

5. Closed-Loop Results

This section provides a comparative analysis of the dynamic response of the dual-rotor OCT under a closed-loop configuration subjected to varying flow speed profiles. The influence of buoyancy control on system performance is evaluated in terms of depth stability, pitch angle dynamics, and electrical power generation, offering insight into the system's behavior under actively regulated operating conditions. The PI controller used in this study is characterized by a proportional gain of $K_p = 150\ \mathrm{m}^{-1}$ and an integral gain of $K_i = 10^{-6}\ (\mathrm{m}\cdot\mathrm{s})^{-1}$, selected to ensure stable and responsive control performance.

In the closed-loop configuration, a PI feedback controller is employed in the OCT to regulate the water fill levels of both fore and aft buoyancy tanks under varying flow speed profiles, ranging from 1.0 m/s to 2.2 $\mathrm{m/s}$, with a turbulence intensity of 10%. All simulations assume an initial equilibrium depth of approximately 75 m and identical ballast tank conditions (each with a 50% fill level) to isolate the influence of flow speed. Fig. 4 illustrates the impact of inflow velocity on the depth, pitch angle, and power generation of the dual-rotor OCT. As shown in Fig. 4 (Top), the depth-time responses demonstrate the effectiveness of the depth controller. For flow speeds between 1.0 and 1.8 $\mathrm{m/s}$, the turbine depth remains close to the target value of 75 m, indicating that the controller compensates for variations in hydrodynamic forces. While gradual sinking is typically expected at lower flow speeds due to insufficient lift, the controller maintains the desired depth. At higher speeds (2.0 and 2.2 $\mathrm{m/s}$), more pronounced oscillations appear, likely due to stronger fluid-structure interaction forces. As shown in Fig. 4 (Middle), the pitch angle response supports these observations. Higher flow speeds produce positive pitch angles (nose-up), while lower speeds result in larger negative pitch angles. Notably, the 1.0 $\mathrm{m/s}$ and 1.2 $\mathrm{m/s}$ cases show nose-down angles around $-10°$, indicating unstable hydrostatic moments. At 2.2 $\mathrm{m/s}$, the pitch stabilizes near $+4°$. Fig. 4 (Bottom) shows that total power generation from both rotors increases with

flow speed. The $1.0\,\mathrm{m/s}$ case stabilizes near 100 kW, while the $2.2\,\mathrm{m/s}$ case reaches nearly 900 kW. At higher flow speeds, more noticeable transient fluctuations are observed before reaching steady-state, likely caused by enhanced fluid-structure interaction.

6. Conclusion

This paper presented a dynamic modeling framework and simulation-based analysis for a dual-rotor ocean current turbine operating under both open-loop and closed-loop conditions. The results highlight the influence of buoyancy tank fill levels, and flow speed on depth regulation, pitch stability, and power generation. These insights support future efforts in control development and system design optimization for reliable and efficient marine energy extraction.

7. Acknowledgments

This work was supported in part by the National Science Foundation under Grant No. CMMI-2145571 and the U.S. Department of Energy (DOE) through the TEAMER program.

References

[1] A. LiVecchi, A. Copping, S. Jenne, A. Gorton, R. Preus, G. Gill, R. Robichaud, R. Green, S. Geerlofs, S. Gore *et al.*, "Powering the blue economy: Exploring opportunities for marine renewable energy in various maritime," National Renewable Energy Laboratory (NREL), Golden, CO (United States), Tech. Rep., 2019.

[2] Y. Tang, J. VanZwieten, B. Dunlap, D. Wilson, C. Sultan, and N. Xiros, "In-stream hydrokinetic turbine fault detection and fault tolerant control-a benchmark model," in *2019 American Control Conference (ACC)*. IEEE, 2019, pp. 4442–4447.

[3] X. Yang, K. A. Haas, and H. M. Fritz, "Evaluating the potential for energy extraction from turbines in the gulf stream system," *Renewable energy*, vol. 72, pp. 12–21, 2014.

[4] Y. Tang, Y. Zhang, A. Hasankhani, and J. VanZwieten, "Adaptive super-twisting sliding mode control for ocean current turbine-driven permanent magnet synchronous generator," in *2020 American Control Conference (ACC)*. IEEE, 2020, pp. 211–217.

[5] J. VanZwieten, F. Driscoll, A. Leonessa, and G. Deane, "Design of a prototype ocean current turbine—part ii: flight control system," *Ocean engineering*, vol. 33, no. 11-12, pp. 1522–1551, 2006.

[6] J. H. VanZwieten, N. Vanrietvelde, and B. L. Hacker, "Numerical simulation of an experimental ocean current turbine," *IEEE Journal of Oceanic Engineering*, vol. 38, no. 1, pp. 131–143, 2012.

[7] A. Hasankhani, J. VanZwieten, Y. Tang, B. Dunlap, A. De Luera, C. Sultan, and N. Xiros, "Modeling and numerical simulation of a buoyancy controlled ocean current turbine," *International Marine Energy Journal*, vol. 4, no. 2, 2021.